remote sensing

MDPI

Technical Note

Observing the Microwave Radiation of the Sun during a Solar Eclipse with a Ground-Based Multichannel Microwave Radiometer

Lianfa Lei [1,2,3,4], Zhenhui Wang [1,2,*], Yingying Ma [5], Jiang Qin [3,4], Lei Zhu [3,4], Rui Chen [3,4] and Jianping Lu [3,4]

1 Collaborative Innovation Center on Forecast and Evaluation of Meteorological Disasters, CMA Key Laboratory of Aerosol-Cloud-Precipitation, Nanjing University of Information Science & Technology, Nanjing 210044, China; leilianfa@nuist.edu.cn or leilianfa_2006@163.com
2 School of Atmospheric Physics, Nanjing University of Information Science & Technology, Nanjing 210044, China
3 North Sky-Dome Information Technology (Xi'an) Co., Ltd., Xi'an 710100, China; qinj2001@163.com (J.Q.); leizhu1202@163.com (L.Z.); chenrui_1978@163.com (R.C.); lujp72@163.com (J.L.)
4 Xi'an Electronic Engineering Research Institute, Xi'an 710100, China
5 State Key Laboratory of Information Engineering in Surveying, Mapping and Remote Sensing (LIESMARS), Wuhan University, Wuhan 430079, China; yym863@whu.edu.cn
* Correspondence: eiap@nuist.edu.cn

Abstract: A ground-based multichannel microwave radiometer (GMR) is commonly used to observe the atmospheric radiation brightness temperature (T_B) in order to retrieve atmospheric temperature and humidity profiles. At present, GMRs are used only in meteorology and climate monitoring. However, theoretical analysis showed that GMRs can be also used to observe the solar radiation. Therefore, we tried to improve the antenna servo control system of a GMR so that it could track and observe the sun, and the results showed that the GMR could respond to the variation of solar radiation. A further question was: can a GMR observe the variation of the sun during a solar eclipse? Fortunately, two solar eclipse events were captured by the GMR on 26 December 2019 and 21 June 2020 in Xi'an, China. We used the upgraded GMR to observe the variation of solar radiation during the two solar eclipses. The observation and analysis results showed that (1) the GMR could accurately track the sun and respond to the variation of solar radiation during the solar eclipse. We analyzed the variation features of the solar radiation by combining the solar phase during the two solar eclipses. (2) We found that the GMR could respond to the variation of the solar radiation arising from the Earth–Sun distance, and we further propose a novel method to measure the eccentricity of earth orbit with the GMR by using the passive solar observation. The results show that the eccentricity measured was 0.0169, which agreed quite well with the value of 0.0167 in the literature. (3) The average variation percentages of both the Earth–Sun distance and the intensity of the incident solar radiation throughout the year were estimated to be 3.44% and 6.6%, respectively. According to these results, the solar observation techniques can broaden the field usage of GMR.

Keywords: microwave radiometer; solar eclipse; solar radiation; eccentricity

check for updates

Citation: Lei, L.; Wang, Z.; Ma, Y.; Qin, J.; Zhu, L.; Chen, R.; Lu, J. Observing the Microwave Radiation of the Sun during a Solar Eclipse with a Ground-Based Multichannel Microwave Radiometer. *Remote Sens.* **2022**, *14*, 2665. https://doi.org/10.3390/rs14112665

Academic Editors: Dimitris Kaskaoutis and Zhenzhan Wang

Received: 19 April 2022
Accepted: 30 May 2022
Published: 2 June 2022

Publisher's Note: MDPI stays neutral with regard to jurisdictional claims in published maps and institutional affiliations.

Copyright: © 2022 by the authors. Licensee MDPI, Basel, Switzerland. This article is an open access article distributed under the terms and conditions of the Creative Commons Attribution (CC BY) license (https://creativecommons.org/licenses/by/4.0/).

1. Introduction

The sun is a natural external source with high radiation intensity, it radiates in a wide frequency band [1], and the solar emission is an approximate blackbody of 6000 to 20,000 K at millimeter and submillimeter wavelengths [2]. Observations of the thermal radio emission of the sun at millimeter wavelengths are important in the evaluation of theoretical atmospheric and surface models [3]. Generally, spectrographs, polarimeters and telescopes are used to observe the solar microwave radiation and activity [3–8], but these devices are generally large, expensive and complicated to operate. The GMR is a typical atmospheric passive remote sensing device, has high sensitivity and it can be also used

to observe the solar radiation. Mattioli et al. (2016) attempted to measure the T_B of solar radiation and propose the parametric retrieval of the atmospheric extinction at 23.8, 31.4, 72.5 and 82.5 GHz [1], but an operational GMR has rarely been used to track and observe solar radiation or a solar eclipse.

At present, as GMRs can continuously observe the atmospheric microwave radiation T_B at K- and V-bands and provide valuable information on the temperature, humidity and liquid water structure of the troposphere [9,10], they have been widely used in meteorology and climate monitoring in last few decades [11–13]. Although there have been some new applications of the technology for radiometers, their applications are limited to atmospheric observation and they are only used to observe and retrieve the temperature and humidity profiles, their value has not been fully utilized in other fields.

Nowadays, new applications have been found for radiometers. For example, based on the theory of atmospheric radiation and the remote sensing potential of GMR, Wang et al. (2014) proposed a method to measure the microwave radiation of a hot air cylinder caused by lightning [14], and Jiang et al. (2018, 2020) observed microwave heating and the duration of artificial rocket-triggered lightning using a GMR [15,16]. In addition, because the sun has strong microwave radiation, theoretical analysis and experimentation show that GMRs are able to observe and monitor solar radiation, and radiometers can be used to observe solar radiation and measure the brightness temperature of solar radiation; the solar monitoring method can be used to measure the antenna pattern, monitor the antenna alignment and evaluate the receiver stability of a GMR in operational field applications [2,17–19]. Therefore, we propose the improvement of the antenna servo control system of a GMR so that it can track and observe the sun automatically, and then attempt to observe the variations of solar radiation. Thus, an operational GMR can be used to observe the T_B variations which reach the antenna due to solar radiation and to study the solar activity and variations of solar radiation [17,18].

A solar eclipse is one of nature's most impressive celestial performances and it happens rarely. So, we wanted to know whether a radiometer could respond to the variation of solar radiation during the solar eclipse. Fortunately, two solar eclipse events happened on 26 December 2019 and 21 June 2020 and were able to be observed in Xi'an, China. The solar eclipses provided a good opportunity for observing the variation of solar radiation. Based on the observation experiment of the sun with a radiometer, we attempted to observe the variation radiation of the sun during the solar eclipse. We monitored the complete duration of solar eclipse with the upgraded GMR, and the results showed that the GMR could respond to the variation of solar radiation and the effective radiation area of the sun during the solar eclipse. More importantly, we successfully observed the variation of the intensity of the solar radiation arising from the Earth–Sun distance and we used these data to evaluate the eccentricity of earth's orbit. The eccentricity is an important astronomical parameter, which may modulate both the earth's magnetic field and climate [20–22].

In this study, we introduced the experiment and theory that the solar eclipse can be remotely sensed with a GMR and attempted to observe the variation radiation of the sun during the solar eclipse. Furthermore, we proposed a novel and simple method to measure the eccentricity of the earth's orbit by using the radiometer to observe the variation of the solar radiation near the perihelion and aphelion. This method does not need complicated astronomical calculation but only observes the variation of solar microwave radiation with a GMR near the perihelion and aphelion. This method is of great significance in real terms. In addition, we also measured the variation percentages of both the Earth–Sun distance and the intensity of the solar radiation. In order to observe solar radiation, solar observations were performed using a GMR installed at the Xi'an field experimental site (34.091°N, E108.89°E) in China. During this experiment, we found that the GMR could be used to monitor the variation radiation of sun and that it could also respond to the variation of the solar radiation arising from the Earth–Sun distance. This solar observation method demonstrates a potential application for GMR and broadens the application field of the radiometer.

2. Theory and Method

2.1. The Observation of the Sun and a Solar Eclipse

In general, a GMR can be used to observe the T_B of the atmosphere. When the antenna is pointed at a certain elevation angle to the sky, the antenna temperature with only the clear sky in the beam can be estimated by [23]:

$$T_{sky}(\theta) = T_{bg}e^{-\tau(\theta)} + T_m\left[1 - e^{-\tau(\theta)}\right], \quad (1)$$

where θ is the observation elevation angle of GMR, T_m is the atmospheric effective temperature and T_{bg} is the cosmic background T_B (T_{bg} = 2.75 K). $\tau(\theta)$ is the atmospheric attenuation at the elevation angle.

When a GMR is used to observe the sun, the T_B measured by the antenna depends on the average solar radiation and the ratio of the solar solid angle to the antenna solid angle and the T_B observation is inversely proportional to the solar solid angle [24]. During the solar eclipse, when the antenna is pointed to the sun, the antenna temperature $T_{sm}(\theta)$ received from both the sun and the moon in the antenna beam would be:

$$T_{sm}(\theta) = T_{bg}e^{-\tau(\theta)} + T_m\left[1 - e^{-\tau(\theta)}\right] + \frac{\Omega_s - \Omega_0}{\Omega_A}\overline{T}_{sun}e^{-\tau(\theta)} + \frac{\Omega_m}{\Omega_A}\overline{T}_{moon}e^{-\tau(\theta)}, \quad (2)$$

where $\overline{T}_{sun}$ and $\overline{T}_{moon}$ are the average T_B for the sun and moon, Ω_m, Ω_s and Ω_A are the solid angles of the moon, the sun and the antenna beam, respectively. Ω_0 is the solid angle of the sun shaded by the moon. Ω_0 equals zero when there is no eclipse and equals the solar solid angle when there is a total solar eclipse. The value of Ω_0 is between (0, Ω_s) for annular or partial eclipse cases.

During observation of the sun, the T_B increment measured by the GMR can be obtained by subtracting (1) from (2),

$$\Delta T'_{sun}(\theta) = [\ \frac{\Omega_s - \Omega_0}{\Omega_A}\overline{T}_{sun} + \frac{\Omega_m}{\Omega_A}\overline{T}_{moon}]e^{-\tau(\theta)}. \quad (3)$$

According to the Equations (1)–(3), when the atmospheric distribution is homogeneous, we can obtain the solar T_B increment by observing the radiation of the sky without the sun and the direction of the sun at same elevation (the solar elevation). When the GMR observes the solar radiation, because of the atmospheric attenuation, the solar radiant energy reaching the earth is reduced. During the observation, the atmospheric attenuation is a key factor and it must be calculated.

The atmospheric attenuation $\tau(\theta)$ can be calculated by using elevation scanning of the sky [23]. After atmospheric opacity calibration, one obtains:

$$\Delta T_{sun} = \frac{\Omega_s - \Omega_0}{\Omega_A}\overline{T}_{sun} + \frac{\Omega_m}{\Omega_A}\overline{T}_{moon}, \quad (4)$$

where ΔT_{sun} is the power from the sun arriving at the antenna without atmospheric attenuation. Considering that $\overline{T}_{sun} \gg \overline{T}_{moon}$, i.e., $\overline{T}_{moon}$ = 0 in Equation (4), one has:

$$\Delta T_{sun} = \frac{\Omega_s - \Omega_0}{\Omega_A}\overline{T}_{sun}. \quad (5)$$

This is the simplified formula for estimating the T_B increment of the sun reaching the antenna during the solar eclipse.

2.2. The Effect of Earth-Sun Distance for the Solar Observation

From Equation (5), when there is no eclipse and the antenna is centered directly towards the sun, the T_B that antenna receives from the sun without atmospheric attenuation can be given as:

$$\Delta T_{sun} = \frac{\Omega_s}{\Omega_A} \overline{T}_{sun}. \tag{6}$$

The solar solid angle would be derived as follows:

$$\Omega_s = 2\pi[1 - \cos(\theta_s)], \tag{7}$$

where θ_s is the angular radius of the sun. For a small angle θ_s, $\cos(\theta_s)$ can be approximated as follows:

$$\cos(\theta_s) \approx 1 - \frac{1}{2}{\theta_s}^2, \tag{8}$$

and θ_s can be given by:

$$\theta_s \approx \frac{r}{d}, \tag{9}$$

where r is the radius of the sun and d is the distance from the sun to the earth. Then the solid angle subtended by the cone given by Equation (7) would be approximately as follows:

$$\Omega_s = \pi \frac{r^2}{d^2}. \tag{10}$$

Then, Equation (6) becomes:

$$\Delta T_{sun} = \frac{\pi}{\Omega_A} \frac{r^2}{d^2} \overline{T}_{sun}. \tag{11}$$

According to Equation (11), the T_B increment is inversely proportional to the square of the distance between the sun and the earth. Since the earth's orbit around the sun is an elliptical and the sun is at one focus of the ellipse, the Earth–Sun distance varies by about 3.4% and the intensity of the solar radiation is 6.5% throughout the year [25]. This is to say that the T_B observation is related to the Earth–Sun distance. The variation of the Earth–Sun distance affects the ratio R of the solar solid angle to the antenna solid angle. If the beam width is known, the ratio R can be calculated accurately. However, as the antenna beamwidth measurement is usually carried out in a microwave anechoic chamber, it is complex and expensive. That being said, antenna pattern measurements with the sun as a signal are widely used by active and passive microwave instruments in meteorology [1,17]. The sun can be assumed to be a point source for the antenna. During the scanning of the sun, the received solar power can be approximated using a Gaussian function. Assuming a Gaussian function for the antenna pattern, the ratio can be approximated as follows [26,27]:

$$R = \frac{\Omega_s}{\Omega_A} = 1 - \exp\left[-4 \ln 2 (\theta_s / \theta_A)^2\right]. \tag{12}$$

Taking into account that the beamwidth of the GMR was less than 5°, we simulated the relationship between the sun filled-beam factor and antenna beamwidth, as shown in Figure 1. The beamwidths of the GMR were around 3~5° at the K-band, and the sun filled-beam factor was less than 0.02. The orbit of the earth is an ellipse and the ratio R is depends on the Earth–Sun distance.

Utilizing Equation (6), we can accurately estimate the T_B increment. For example, when the antenna beamwidth is 4.5°, the calculation results show that the variation of the T_B increment is about 3 K throughout the year, and the variation is more obvious with a narrower beamwidth. The sensitivity for most GMRs for meteorological applications consists of less than 0.3 K in 1 s of integration time and therefore it is certain that a radiometer is capable of precise measurements of the annual variation of T_B increment.

During observation, we can ignore the variation of the T_B increment due to sun movements in 1 s of integration time.

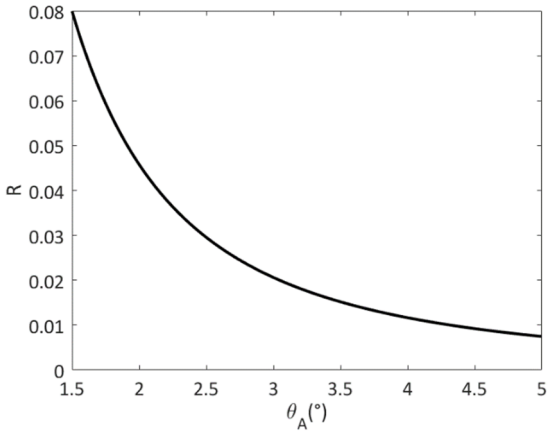

Figure 1. The relationship between the sun filled-beam efficiency and beamwidth.

2.3. Measuring Eccentricity of the Earth Orbit

According to the observation results, a GMR can respond to the variation of the solar radiation arising from the Earth–Sun distance, and, therefore, we propose a new method to calculate the eccentricity of the earth's orbit by using the observed solar microwave radiation T_B with a GMR when the earth is near the perihelion and aphelion. This method is simple and does not require complicated observations and mathematical calculations.

For an elliptic orbit, the eccentricity e is given by:

$$e = \frac{c}{a}, \tag{13}$$

where a is the length of the semi-major axis, c is the semi-distance between the two foci. When the earth is at the perihelion and aphelion, the distance between earth and sun is $a - c$ and $a + c$, respectively. According to Equations (11) and (12), one has

$$\frac{\Delta T_{sun}^{p}}{\Delta T_{sun}^{a}} = \frac{(a+c)^2}{(a-c)^2} = \frac{(1+e)^2}{(1-e)^2}, \tag{14}$$

where ΔT_{sun}^{p} and ΔT_{sun}^{a} are the T_B increment when the earth is at the perihelion and aphelion. Let $M = \frac{\Delta T_{sun}^{p}}{\Delta T_{sun}^{a}}$, and one has

$$e = \frac{\sqrt{M}-1}{\sqrt{M}+1}, \tag{15}$$

and

$$Q = \left(\frac{a+c}{a-c} - 1\right) \times 100\% = \left(\sqrt{M} - 1\right) \times 100\%, \tag{16}$$

$$R = \left(1 - \frac{1}{M}\right) \times 100\% \tag{17}$$

where Q represents the percentage of the variation of the Earth–Sun distance, and R represents the percentage of the variation of the solar radiation intensity.

3. Instrument and Experiments

3.1. The Radiometer and Observation Mode

The GMR (model MWP967KV) used for this experiment, shown in Figure 2, was developed and manufactured by our research team. It is a passive remote sensing instrument

that measures the atmospheric radiation to retrieve temperature, humidity and liquid water profiles as well as integrated water vapor and liquid water paths in real time.

The GMR usually measures T_B in the K-band (22–30 GHz) and V-band (51–59 GHz). It is comprised of an antenna system and two sensitive heterodyne receivers as well as a detector unit and data retrieval system. It contains a high-precision elevation and azimuth-stepping scanning system to scan the sky, and the angle resolution is 0.1°. The receiver system consists of two super-heterodyne receivers covering K- and V-bands, each band is independently received and detected, and all channels use a common local oscillator signal. The antenna system contains a parabolic reflector, beam splitter and compactness a corrugated feed-horn. In addition, it is calibrated by using liquid nitrogen (LN2), hot load, a noise diode and the tipping curve method. During observations, the GMR underwent regular maintenance and the LN2 calibrations were performed twice a year. The system performance parameters are given in Table 1.

Figure 2. The multichannel microwave radiometer used for this experiment.

Table 1. The system performance of the GMR used in this study.

Parameter	Specification
Frequency	K-band (22~30 GHz); V-band (51~59 GHz)
Beam width	K-band: ≤5°; V-band: ≤3°
Gain	≥25 dB
Sidelobe level	≤−25 dB
Brightness temperature accuracy	0.5 K
Brightness temperature sensitivity	K-band: ≤0.25 K (RMS); V-band: ≤0.3 K (RMS);
Integration time	Typically, 1 s
Antenna azimuth and elevation scanning	+/−180° stepping scanning
Antenna angular resolution	0.1°
Calibration method	Hot load; Noise diode; Tipping method; LN2

In order to track and observe the sun, the antenna servo control system was improved so that the GMR could be adjusted to control its antenna beam to scan the sun. When the GMR tracked and observed the sun, we were easily able to obtain the T_B variation from the sun arriving at the antenna and thus study the solar activity.

The upgraded GMR was set up at the Xi'an field experiment site (34.091°N, 108.89°E). The GMR works on two modes, the meteorological observation mode and the solar observation mode.

(1) Meteorological observation mode. Generally, the GMR adopts meteorological observation mode to obtain atmospheric T_Bs which are used to retrieve atmospheric temperature and humidity profiles.
(2) The solar observation mode. This observation mode was developed and was used to track and remotely observe solar radiation. Firstly, the antenna system was adjusted to point towards the center of the sun and then the antenna beam was tuned to scan the sun using a polar plane indicator (PPI) by adding a step value on the antenna azimuth. Secondly, the antenna was adjusted so that the sun was completely out of the beam in order to scan the sky using a range height indicator (RHI) by adding a step value to the antenna elevation, then the antenna was moved from the sun in order to obtain the sky background radiation as a reference and to calculate the atmospheric opacity with the tipping calibration method. Finally, we obtained the T_B increment of the sun without the atmospheric attenuation by utilizing Equations (1) to (5). This scanning can last up to 3 min for each observation, depending on the scanning step angle count.

Since the sun moves through the sky within this time interval, in order to reduce errors, the antenna direction also follows the sun. We needed to recalculate the solar azimuth and elevation prior to changing the antenna pointing position in real-time, and the azimuth and elevation step angles are the relative angle between the antenna beam direction and the sun; this relative angle was fixed for each observation. Common scan parameters are listed in Table 2.

When tuning the antenna beam to scan the sun in the azimuth, a rotation of the antenna in the azimuth with a constant elevation does not describe a great circle on the sky-sphere, there were some distortions [1]. There is an extreme case when the azimuth of the antenna is rotated at an elevation angle of 90°, but the antenna beam pointing would not move on the sky. For the distortion and the calibration method, Reimann and Hagen (2016) described it in detail [1]. We calculated the distortion angle by using their method. If we had not calibrated the angle distortion, it would have caused a large bias in the beamwidth measurement.

Table 2. Scan parameters used for sun measurements.

Parameter	Specification
Frequencies for solar observation	22.235, 25.0, 30.0 GHz
Antenna scanning type	PPI/RHI
Scanning position	Around the sun as the center
Azimuth scanning range	−10°~10°
Azimuth scanning step	0, ±0.1, ±0.25, ±0.5, ±1, ±1.5, ±2, ±2.5, ±3, ±4, ±5, ±6, ±7, ±8, ±10°
Sky elevation scanning	Elevation: 30, 45, 60, 90, 120, 135, 150°
Integration time	Typically, 1 s
Scanning time	~3 min

3.2. The Solar Eclipse Events

Solar eclipses rarely happen, but fortunately we witnessed two partial solar eclipses on 26 December 2019 and 21 June 2020 in Xi'an, China. These partial eclipses were visible in most parts of China. However, an annular solar eclipse was also seen in some areas of China on 21 June 2020, the annular phase of this eclipse was visible from a narrow part of southern of China (darker shaded area in the map below). In the lighter shaded areas, the partial solar eclipse was visible. Figure 3 shows the path of the eclipse shadow and the percentage of maximum obscuration, the two maps show the visibility of the annular solar eclipse on 26 December 2019 and 21 June 2020, and stages and times of the eclipse events observed by this study are summarized in Table 3 (for details, see: https://www.timeanddate.com/eclipse (accessed on 10 October 2020)).

During a solar eclipse, because the sun is shaded by the moon, the radiant energy reaching the earth is reduced. Therefore, the variations of solar radiation can be observed

by a GMR. In order to trace and observe the process of the solar eclipse, we improved and developed a solar observation mode so that it could track and observe the sun, and we used the upgraded GMR to observe the variation of solar radiation. Fortunately, the two solar eclipse events were captured by our GMR; the sun was tracked and scanned at three frequencies (22.235, 25.0, 30.0 GHz) in K-band on 26 December 2019 and 21 June 2020, and the progress of the two solar eclipses was observed and recorded with the GMR during the period of the two eclipses.

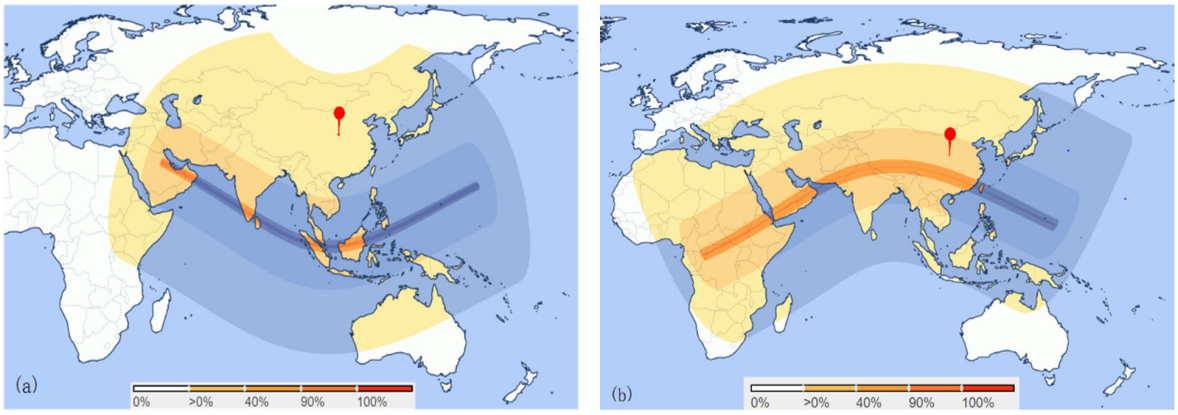

Figure 3. The portion of the sun covered by the moon (eclipse obscuration) and the red marker represents the observation site in Xi'an, China. (**a**) 26 December 2019, (**b**) 21 June 2020.

Table 3. Stages and times of the eclipse events outlined for Xi'an (all times were local time, CST).

Eclipse Time	First Contact	Maximum Phase	Last Contact	Duration	Max-Obscuration
26 December 2019	12:21	13:29	14:36	2 h 15 min	11.4%
21 June 2020	14:16	15:47	17:06	2 h 50 min	74.9%

4. Discussion

4.1. The Scanning Data Analysis during the Two Solar Eclipses

During the scanning of the sun, the sun can be assumed to be a point source for the antenna, the solar T_B increment received by the antenna can be assumed to be a Gaussian function of the radial distance to the antenna beam axis [4,27]. The T_B increment is given by:

$$\Delta T_{sun}(x) = A_d \exp[-4 \ln 2 \left(\frac{x}{\theta_A} \right)^2], \quad (18)$$

where x is the angle radius distance from the sun to the center of the antenna beam, θ_A is the antenna half-power beamwidth, and A_d is the maximum T_B increment when the antenna is pointing to the center of the sun. During scanning data by the GMR, the antenna beamwidth and the maximum T_B increment can be easily fitted by the least-square method. That is to say that the sun can be used to measure the antenna pattern of the radiometer. The measurement of principle and method have already been reported in detail in previous papers [17,18].

We used the upgraded radiometer to track and scan the sun during the two solar eclipses. The GMR recorded the variation of the T_B at three frequencies (22.235, 25.0, 30.0 GHz) in K-band on 26 December 2019 and 21 June 2020. These two eclipses provided a very good opportunity for us to observe the solar eclipse process with a microwave radiometer. In order to compare the variation of solar radiation T_B, we also scanned and observed the solar T_B without solar eclipse. During the process of scanning the solar eclipse, we measured T_B increments at many step angles at three frequencies after correction for the angle distortion, as is shown in Figures 4 and 5 for 26 December 2019 and 21 June 2020,

respectively. The observation results showed that the solar eclipse could be observed by the GMR. According to Equation (17), the scanning data were fitted with Gaussian function using the least squares fitting, and the statistical results are given in Table 4. The results showed that:

(1) the scanning points near the sun showed good symmetry and consistency with the results from a fitting using the Gaussian function. The scanning data were able to be used to measure the antenna pattern;
(2) the maximum value of T_B increment was different for each frequency, but they were related to the antenna beamwidth, and the fitting of beamwidth (β) was not affected by solar eclipse (see Table 4). Because the Earth–Sun distance is very far, the sun can be regarded as a point source during the solar eclipse. Therefore, it did not affect the measurement of antenna beamwidth;
(3) during the solar eclipse, the T_B increment decreased significantly when compared to the main beam without the solar eclipse, because the sun disk was shaded by the moon and the level of solar radiation became small;
(4) the T_B increment was related to the portion of the sun shaded by the moon, when the solar eclipse reached its maximum phase, the decrease of the T_B increment was at its maximum;
(5) because of the variations of the Earth–Sun distance, the T_B observed by radiometer is different at different times.

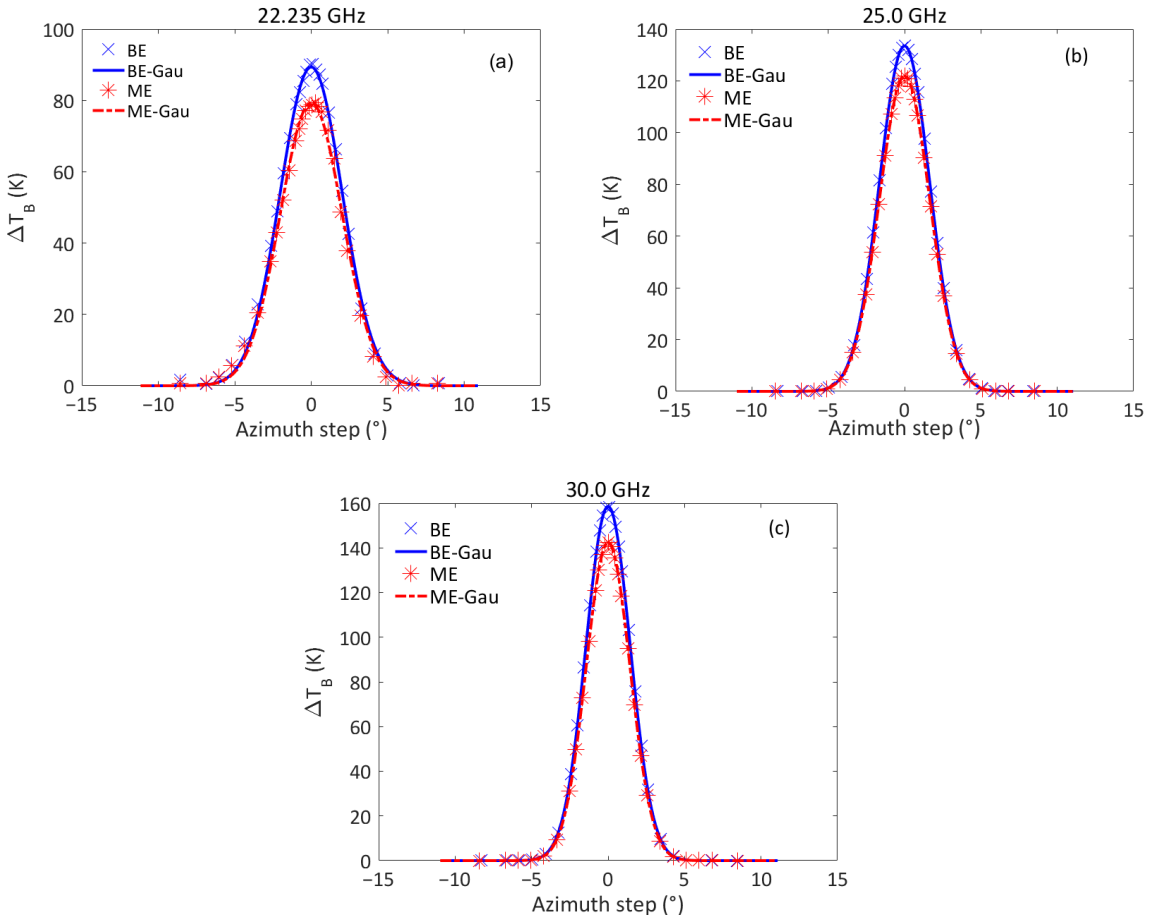

Figure 4. The variation of T_B increment during the scanning of the sun at the azimuth on 26 December 2019. BE means "before eclipse" and ME means "maximum eclipse". The dots are observed data and the line is a fitting of the Gaussian function (Gau). (**a**) 22.235 GHz, (**b**) 25.0 GHz, (**c**) 30.0 GHz.

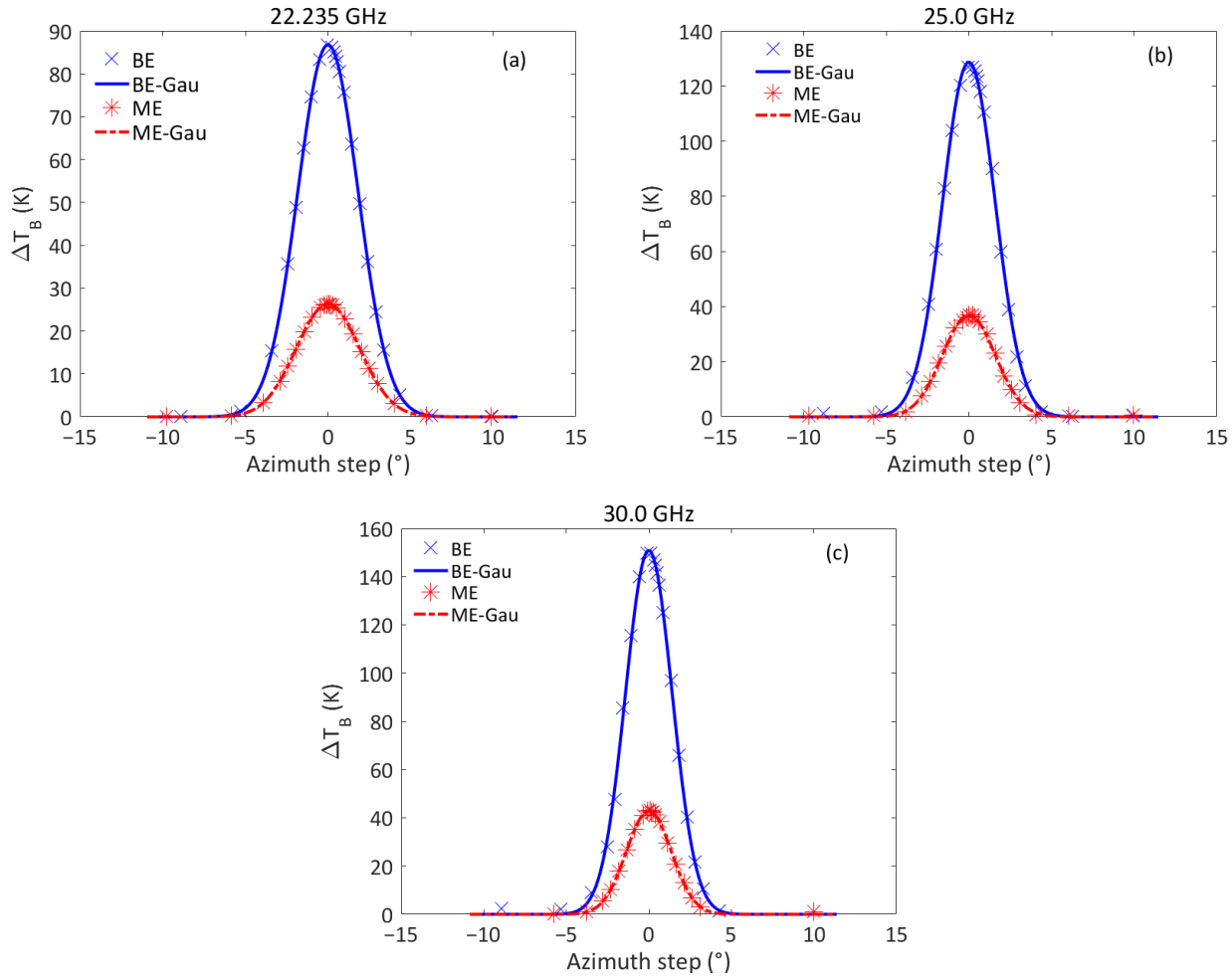

Figure 5. The variation of T_B increment during the scanning of the sun at the azimuth on 21 Jun 2020. BE means "before eclipse" and ME means "maximum eclipse". The dots are observed data and the line is a fitting of the Gaussian function (Gau). (**a**) 22.235 GHz, (**b**) 25.0 GHz, (**c**) 30.0 GHz.

Table 4. The parameters obtained by curve fitting with the Gaussian function at each of the three frequencies. BE means "before eclipse" and ME means "maximum eclipse".

Date	Eclipse Phase	Ad (K)			β (°)		
		22.235 GHz	25.0 GHz	30.0 GHz	22.235 GHz	25.0 GHz	30.0 GHz
26 December 2019	BE	89.4	136.4	157.7	4.6	3.9	3.3
	ME	79.2	121.1	142.3	4.7	3.8	3.4
21 June 2020	BE	86.1	127.6	150.3	4.6	3.7	3.4
	ME	29.8	44.7	52.5	4.6	3.9	3.3

4.2. The Process and Characteristics of a Solar Eclipse

Our study was based on the measurements from the GMR on the day of eclipse and several days before and after eclipse occurred. During a solar eclipse, the sun might be totally or partially shaded by the moon, which could affect the irradiance level from the sun. Therefore, we tried to use the radiometer to observe the process of a solar eclipse. To describe the solar eclipse, we accurately calculated the eclipse obscuration, and it was determined as a covered-to-total solar disc surface ratio [28,29]. The non-covered ratio is shown with a blue dash line in Figures 6 and 7 for 26 December 2019 and 21 June 2020, respectively.

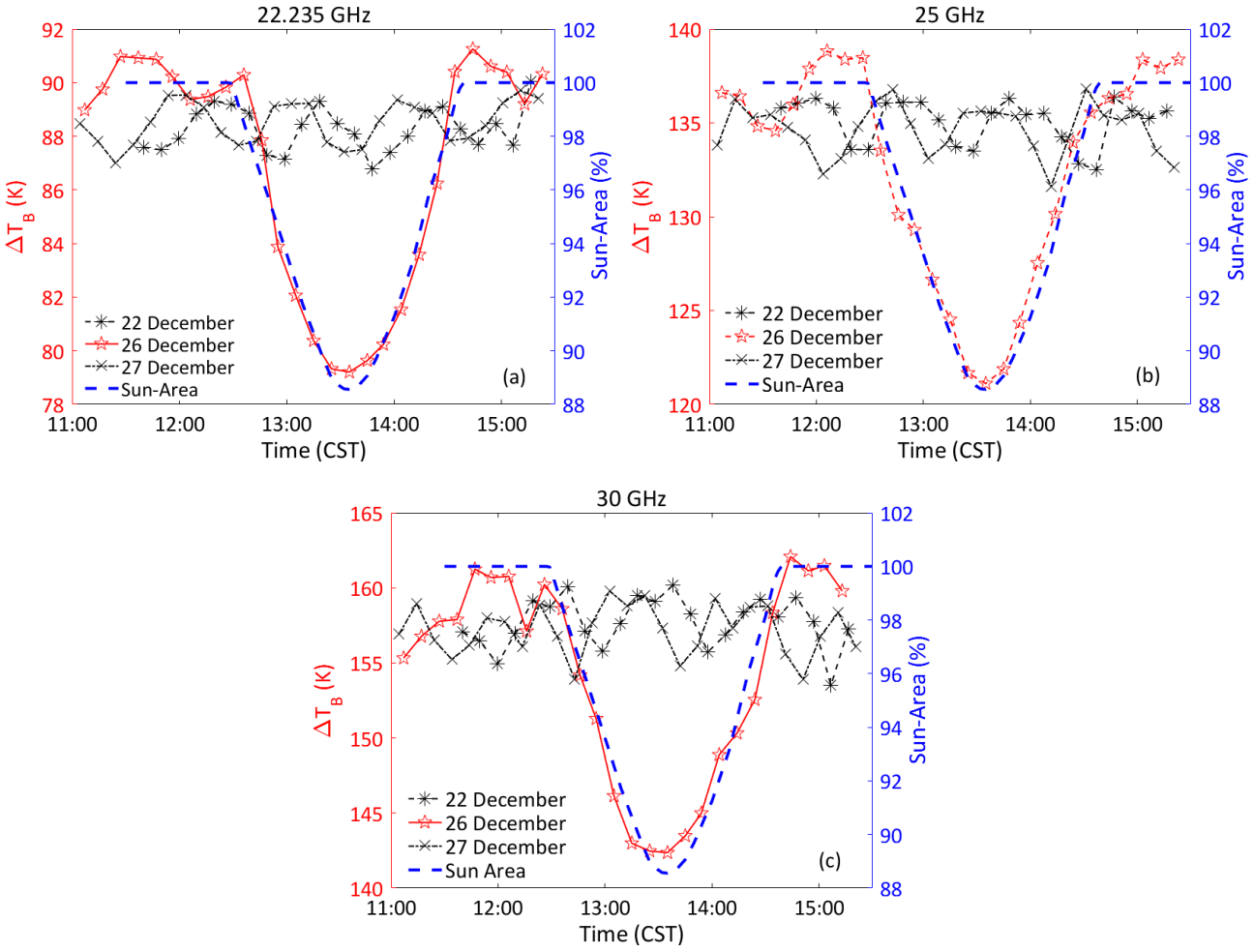

Figure 6. The variation of the T_B increment (left axis) during the solar eclipse on 26 December 2019 (red solid curve with ☆ marks) as compared with that before and after the solar eclipse on 22 December and 27 December (black curve with other marks). All times were local times (CST). The blue dash line represents the percentage of the unshaded solar disk area (right axis). (**a**) 22.235 GHz; (**b**) 25.0 GHz; (**c**) 30.0 GHz.

We calculated and analyzed the T_B increment of the sun as it reached the GMR antenna. The relationship between the eclipse obscuration and the T_B increment are also shown in Figures 6 and 7, the signed line curve gives the experimentally observed values, and we tried to achieve the closest agreement between the observed and theoretical eclipse curves. In order to compare the change between the eclipse obscuration and the T_B increment, we also provided the non-eclipse observation data. According to our observations, a good agreement between the calculated non-covered ratio curve and the observed eclipse curves were found at every frequency. Normally, the T_B increment had no obvious fluctuation during non-eclipse conditions, but the solar eclipse started to affect the T_B increment when it initially occurred (first contact), and this effect disappeared at last contact. The observation results showed that the T_B increment was at a minimum when the shadow area was at a maximum.

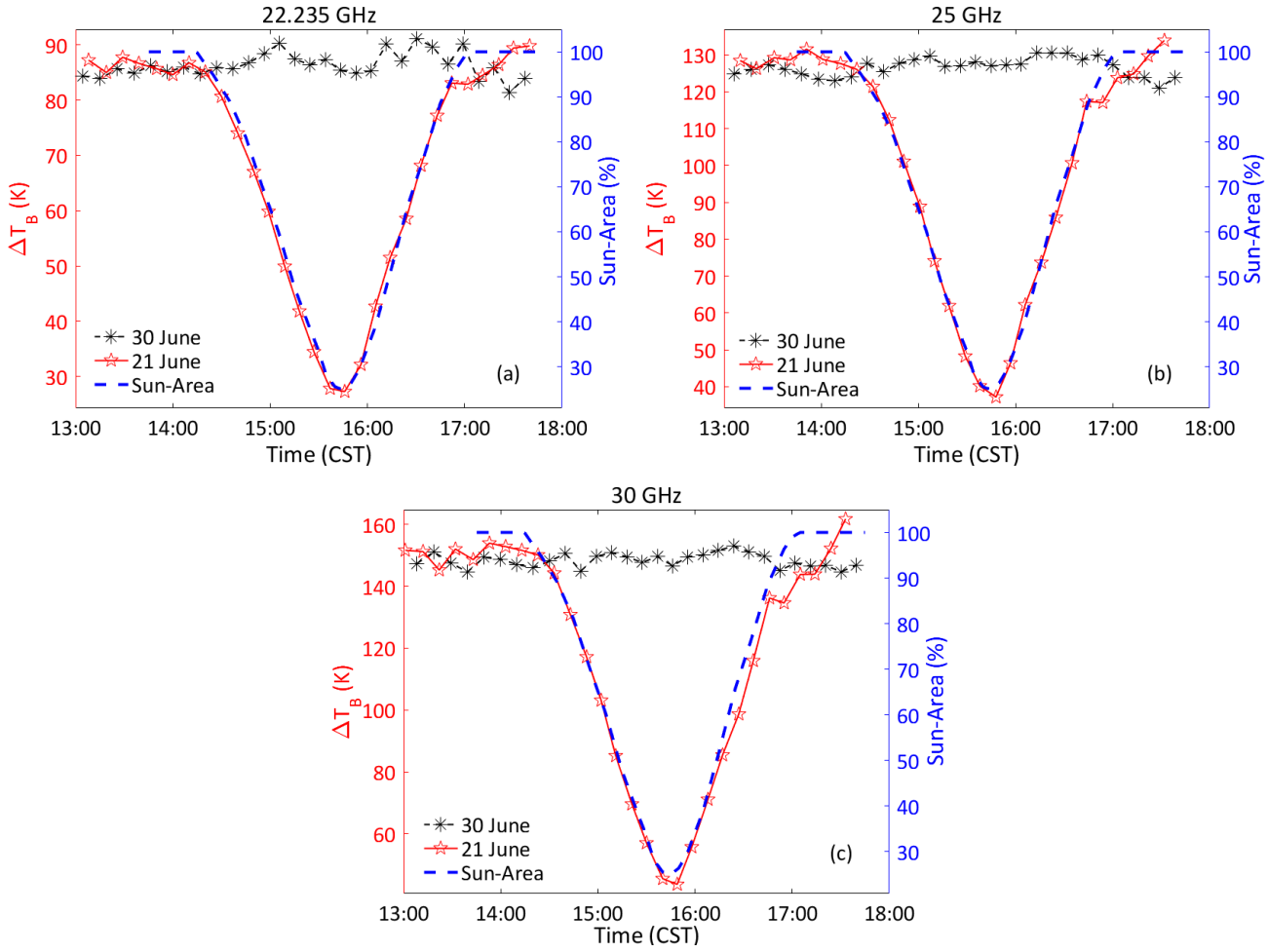

Figure 7. The variation of the T_B increment (left axis) during the solar eclipse on 21 June 2020 (red solid curve with ☆ marks) as compared with that after the solar eclipse on 30 June (black curve with * marks). The blue dash line represents the percentage of the unshaded solar disk area (right axis). (**a**) 22.235 GHz, (**b**) 25.0 GHz, (**c**) 30.0 GHz.

4.3. The Effect of the Earth-Sun Distance to TB Increment

The orbit of the earth is an ellipse, as can be seen from the distance between the sun and the earth at the perihelion and aphelion. There is periodic variation for Earth–Sun distance, and the angular radius of the sun depends on the distance. According to the Equations (10) and (11), the Earth–Sun distance determines the ratio of solar solid angle of the antenna beam. During the solar observation, the earth is near at perihelion in early January, when the sun is closest to the earth, and the solar solid angle is near the maximum and the average radiation T_B increment received by the antenna is at its maximum. However, in early July, when the sun is farthest from the earth, the solar solid angle is the smallest in the year, and the average radiation T_B increment received by the antenna is also at a minimum.

According to this theory, we analyzed the observed solar radiation T_B without a solar eclipse and the results showed that the T_B increment was also variable at three frequencies when there was no eclipse, as shown by Figure 8. The earth was near the perihelion on 27 December 2019 and 1 January 2020, and the average radiation T_B increment received by the GMR was at a maximum and the earth was farthest from the sun on 30 June and 2 July 2020, where the average radiation T_B increment received by the GMR was at a minimum. The average percentage of the T_B variation was 6.6% at three frequencies. These observation data indicate the variation of the Earth–Sun distance. The statistical results are given in Table 5.

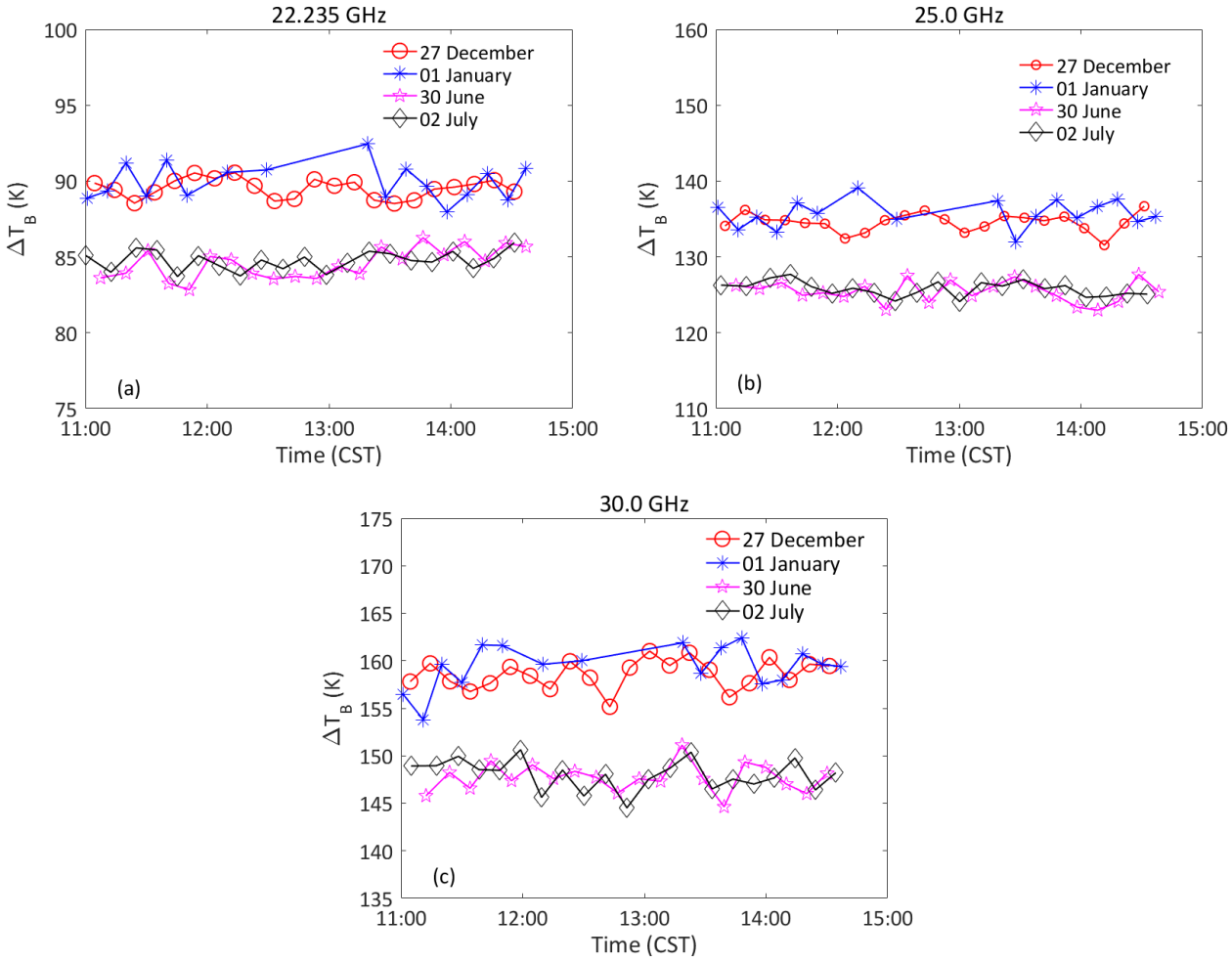

Figure 8. The variation of the T_B increment as a function of time before the solar eclipse on 26 December 2019 and 21 June 2020 (red curve) as compared with that after the solar eclipse on 27 December 2019 and 30 June 2020 (blue curve). (**a**) 22.235 GHz, (**b**) 25.0 GHz, (**c**) 30.0 GHz.

Table 5. Average T_B increment during non-eclipse conditions.

Date	Average ΔT_{sun} (K)		
	22.235 GHz	**25.0 GHz**	**30.0 GHz**
27 December 2019	90.2 ± 0.6	134.3 ± 1.2	157.6 ± 1.6
1 January 2020	90.5 ± 1.6	135.1 ± 1.9	158.7 ± 2.1
30 June 2020	84.5 ± 1.1	125.5 ± 1.7	147.4 ± 1.8
2 July 2020	84.3 ± 0.6	126.3 ± 1.0	147.9 ± 1.5

4.4. Measuring the Eccentricity of the Earth's Orbit

During observation of the sun, we obtained the T_B increments observed on 27 December 2019, 1 January 2020, 30 June 2020, and 2 July 2020, which are quite close to the perihelion and aphelion; the statistical results are shown in Table 5. From Equation (14) to Equation (17), the T_B increments observed on the perihelion and aphelion days could be used to calculate the values of e, Q and R, which were 0.0169, 3.44% and 6.6%, respectively. These results were consistent with previous studies [25,30]. We can see that the average eccentricity estimated is relatively in good agreement with the 0.0167 given in the literature. The average variation of the Earth–Sun distance is 3.44% throughout the year. The intensity of the incident solar radiation at the aphelion should be about 6.6% less than at the perihelion.

This method broadens the field usage of GMR, and it shows that the GMR can be used to measure the eccentricity of earth orbit accurately and even to monitor the variation of the solar radiation. The measurements of the solar T_B increment and eccentricity both depend on antenna errors, regarding its pointing towards the sun, and observation errors. Therefore, these effects have to be taken into account during observation and calibration. In order to reduce the observation error, the GMR underwent regular maintenance and the LN2 calibrations were performed twice a year.

The antenna direction is an important factor of the observations, and it has to be calibrated. During the scanning observation, the maximum T_B increment can be received by the GMR when the antenna beam points to the center of the sun, and the biases of the antenna beam pointing between the peak T_B and the predicted sun position can be used to calibrate the antenna direction [17]. In addition, solar activity may be a factor influencing the observation results, an effect which we will study further though future long-term observation.

5. Conclusions

The microwave T_B observation experiment with the upgraded GMR was carried out at the Xi'an field experiment site, where we made an attempt to observe the sun with a GMR. The two solar eclipse events happened on 26 December 2019 and on 21 June 2020 and were observed at three frequencies (22.235, 25.0 and 30.0 GHz). We observed and studied the variation of the intensity of the solar radiation arising from the eccentricity of the earth's orbit with the GMR for the first time, and the results from the data analysis were herein presented.

(1) We provided a new method to observe and monitor the process of the solar eclipse with a GMR. This method develops and extends the application possibilities of the GMR. The observation results showed that the GMR can accurately respond to the variations of solar radiation, and we analyzed the variation features of solar radiation by combining the solar phase during two solar eclipses. During the solar eclipse, the effective radiation region of the sun was shadowed by the moon and the observed T_B increment were in good agreement with the percentage of the shadow of the solar eclipse. The two solar eclipses gave us the unique possibility to observe and study the varying features of solar radiation.

(2) More importantly, we found that the GMR could respond to the variation of the solar radiation arising from the Earth–Sun distance. Therefore, a good experimental determination of the eccentricity of earth orbit by using GMR has been described and the estimated eccentricity of the earth's orbit is 0.0169, which is in relatively good agreement with the 0.0167 found in the literature.

(3) In addition, we also estimated the average variation of the Earth–Sun distance and the intensity of the incident solar radiation with the GMR, and the results showed that the variations are 3.44% and 6.6% throughout the year, which supports previous theoretical and observational results.

In future work, we will continue to observe the long-term variation of the solar microwave radiation with the GMR, so that a possible study regarding the features of solar activity and their effects on the earth's atmosphere can be carried out.

Author Contributions: Conceptualization, L.L., J.L. and Z.W.; methodology, L.L., J.L., Z.W. and Y.M.; software, L.L.; validation, L.L., L.Z., R.C. and J.Q.; formal analysis, L.L. and Y.M.; resources, L.Z. and R.C.; data curation, L.L.; writing—original draft preparation, L.L., Z.W. and Y.M.; writing—review and editing, L.L., Y.M. and Z.W.; project administration, Z.W. and J.L.; funding acquisition, Z.W. All authors have read and agreed to the published version of the manuscript.

Funding: This research was funded by the National Natural Science Foundation of China (NO. 41675028), the Natural Science Foundation of Shanxi Province, China (NO. 2020JM-718), the Xi'an Science and Technology Project of Shanxi Province, China (NO. 20SFSF0015).

Data Availability Statement: The data presented in this study are available on request from the corresponding author.

Acknowledgments: We are grateful to the Shanxi Provincial Atmospheric Sounding Technical Support Center and the Xi'an Meteorological Observation Center of Shaanxi Province, China, for the radiometer installation and for their support.

Conflicts of Interest: The authors declare no conflict of interest.

References

1. Reimann, J.; Hagen, M. Antenna Pattern Measurements of Weather Radars Using the Sun and a Point Source. *J. Atmos. Ocean. Technol.* **2016**, *33*, 891–898. [CrossRef]
2. Mattioli, V.; Milani, L.; Magde, K.M.; Brost, G.A.; Marzano, F.S. Retrieval of Sun Brightness Temperature and Precipitating Cloud Extinction Using Ground-Based Sun-Tracking Microwave Radiometry. *IEEE J. Sel. Top. Appl. Earth Obs. Remote. Sens.* **2016**, *10*, 3134–3147. [CrossRef]
3. Ulich, B.L. Absolute brightness temperature measurements at 2.1-mm wavelength. *Icarus* **1974**, *21*, 254–261. [CrossRef]
4. Ulich, B.; Haast, R. Absolute calibration of millimeter-wavelength spectral line. *Astrophys. J. Suppl. Ser.* **1976**, *30*, 247–258. [CrossRef]
5. Covington, A.E. Micro-Wave Solar Noise Observations During the Partial Eclipse of November 23, 1946. *Nature* **1947**, *159*, 405–406. [CrossRef]
6. Kaufmann, P.; Scalise, E.; Santos, P.M.D.; Schaal, R.E.; Fortunato, R.A.A. Microwave observations of the 4 January 1973 solar eclipse. *Sol. Phys.* **1973**, *33*, 69–73. [CrossRef]
7. Chatterjee, T.N.; Datta, S.K.; Chatterjee, S.; Tarafdar, G.; Bera, J.; Rahman, M.; Bera, M.; Mitra, A.; Karmakar, P.K. Observation of microwave radio Sun during total solar eclipse on October 24, 1995 by Eastern Centre for Research in Astrophysics (ECRA). *Indian J. Phys.* **1996**, *70B*, 169–173.
8. Sawant, H.S.; Srivastava, N.; Trigoso, H.E.; Sobral, J.H.A.; Femandes, F.C.R.; Cecatto, J.R.; Subramanian, K.R. Radio Observation of Total Solar Eclipse of November 3, 1994 at Chapecoó (BRZIL). *Adv. Space Res.* **1997**, *20*, 2359–2363. [CrossRef]
9. Ahn, M.-H.; Won, H.Y.; Han, D.; Kim, Y.-H.; Ha, J.-C. Characterization of downwelling radiance measured from a ground-based microwave radiometer using numerical weather prediction model data. *Atmos. Meas. Tech.* **2016**, *9*, 281–293. [CrossRef]
10. Bianco, L.; Friedrich, K.; Wilczak, J.M.; Hazen, D.; Wolfe, D.; Delgado, R.; Lundquist, J.K. Assessing the accuracy of microwave radiometers and radio acoustic sounding systems for wind energy applications. *Atmos. Meas. Tech.* **2017**, *10*, 1707–1721. [CrossRef]
11. Cadeddu, M.P.; Liljegren, J.C.; Turner, D.D. The atmospheric radiation measurement (ARM) program network of microwave radiometers: Instrumentation, data, and retrievals. *Atmos. Meas. Tech.* **2013**, *6*, 2359–2372. [CrossRef]
12. Xu, G.; Xi, B.; Zhang, W.; Cui, C.; Dong, X.; Liu, Y.; Yan, G. Comparison of atmospheric profiles between microwave radiometer retrievals and radiosonde soundings. *J. Geophys. Res. Atmos.* **2015**, *120*, 10313–10323. [CrossRef]
13. Yang, J.; Min, Q. Retrieval of atmospheric profiles in the New York State Mesonet using one-dimensional variational algorithm. *J. Geophys. Res. Atmos.* **2018**, *123*, 7563–7575. [CrossRef]
14. Wang, Z.; Li, Q.; Hu, F.; Cao, X.; Chu, Y. Remote sensing of lightning by a ground-based microwave radiometer. *Atmos. Res.* **2014**, *150*, 143–150. [CrossRef]
15. Jiang, S.; Pan, Y.; Lei, L.; Ma, L.; Li, Q.; Wang, Z. Remote sensing of the lightning heating effect duration with ground-based microwave radiometer. *Atmos. Res.* **2018**, *205*, 26–32. [CrossRef]
16. Jiang, S.; Wang, Z.; Lei, L.; Pan, Y.; Lyu, W.; Zhang, Y. Preliminary study on the relationship between the brightness temperature pulses observed with a ground-based microwave radiometer and the lightning current integral values. *Atmos. Res.* **2020**, *245*, 105072. [CrossRef]
17. Lei, L.; Wang, Z.; Qin, J.; Zhu, L.; Chen, R.; Lu, J.; Ma, Y. Feasibility for Operationally Monitoring Ground-Based Multichannel Microwave Radiometer by Using Solar Observations. *Atmosphere* **2021**, *12*, 447. [CrossRef]
18. Lei, L.; Wang, Z.; Ma, Y.; Zhu, L.; Qin, J.; Chen, R.; Lu, J. Measurement of Solar Absolute Brightness Temperature Using a Ground-Based Multichannel Microwave Radiometer. *Remote Sens.* **2021**, *13*, 2968. [CrossRef]
19. Marzano, F.S.; Mattioli, V.; Milani, L.; Magde, K.M.; Brost, G.A. Sun-Tracking Microwave Radiometry: All-Weather Estimation of Atmospheric Path Attenuation at Ka-, V-, and W-Band. *IEEE Trans. Antennas Propag.* **2016**, *64*, 4815–4827. [CrossRef]
20. Wollin, G.; Ryan, W.B.F.; Ericson, D.B.; Foster, J.H. Paleoclimate, paleomagnetism and the eccentricity of the Earth's orbit. *Geophys. Res. Lett.* **1977**, *4*, 267–270. [CrossRef]
21. Bertrand, C.; Loutre, M.F.; Berger, A. High frequency variations of the Earth's orbital parameters and climate change. *Geophys. Res. Lett.* **2002**, *29*, 40-1–40-4. [CrossRef]
22. Rial, J.A. Earth's orbital eccentricity and rhythm of the Pleistocene ice ages: The concealed pacemaker. *Glob. Planet. Change* **2004**, *41*, 81–93. [CrossRef]
23. Han, Y.; Westwater, E.R. Analysis and Improvement of Tipping Calibration for Ground-Based Microwave Radiometers. *IEEE Trans. Geosci. Remote Sens.* **2000**, *38*, 1260–1276. [CrossRef]
24. Coates, R. Measurements of Solar Radiation and Atmospheric Attenuation at 4.3-Millimeters Wavelength. *Proc. IRE* **1958**, *46*, 122–126. [CrossRef]

25. Das Gupta, M.K.; Basu, D. Effect of the earth's orbital eccentricity on incident solar flux at 10·7 cm. *J. Atmos. Terr. Phys.* **1964**, *26*, 135–137. [CrossRef]
26. Ulich, B. A radiometric antenna gain calibration method. *IEEE Trans. Antennas Propag.* **1977**, *25*, 218–223. [CrossRef]
27. Holleman, I.; Huuskonen, A.; Kurri, M.; Beekhuis, H. Operational Monitoring of Weather Radar Receiving Chain Using the Sun. *J. Atmos. Ocean. Technol.* **2010**, *27*, 159–166. [CrossRef]
28. Szałowski, K. The effect of the solar eclipse on the air temperature near the ground. *J. Atmos. Sol.-Terr. Phys.* **2002**, *64*, 1589–1600. [CrossRef]
29. Reda, I. Solar eclipse monitoring for solar energy applications. *Sol. Energy* **2015**, *112*, 339–350. [CrossRef]
30. Lahaye, T. Measuring the eccentricity of the Earth's orbit with a nail and a piece of plywood. *Eur. J. Phys.* **2012**, *33*, 1167–1178. [CrossRef]